Neutron holography and diffuse scattering of palladium hydride

Kouichi Hayashi,[1,*] Kenji Ohoyama,[1,2] Shin-ichi Orimo,[1,2] Hideyuki Takahashi,[3] and Kaoru Shibata[4]

[1]*Center of Neutron Science for Advanced Materials, Institute for Materials Research, Tohoku University, Sendai 980-8577, Japan*

[2]*WPI-Advanced Institute for Materials Research, Tohoku University, Sendai 980-8577, Japan*

[3]*Graduate School for Environmental Science, Tohoku University, Sendai 980-8579, Japan*

[4]*J-PARC Center, Japan Atomic Energy Agency, Tokai, Ibaraki 319-1195, Japan*

(Received 26 August 2013; revised manuscript received 3 December 2014; published 7 January 2015)

To extract a pure atomic-resolution hologram around hydrogen from a two-dimensional (2D) neutron intensity distribution around a single crystal, enhancement of the holographic signal and suppression of the diffuse scattering are important; sample cooling can achieve both. To estimate the performance of sample cooling in achieving these requirements, the angular anisotropy of the neutron intensities around a $PdH_{0.78}$ single crystal was measured at 300 K and 100 K. In addition to the reduction in the diffuse scattering intensity, the pattern itself changed markedly upon sample cooling, thus indicating a significant modification of the hydrogen lattice dynamics. The reconstruction from a hologram, which was obtained by subtracting the diffuse scattering pattern, shows images of H and Pd nuclei as negative and positive peaks, respectively. In particular, such reconstruction at 100 K exhibits distinct H images at distant positions owing to the suppression of hydrogen motion. These features are important for the determination of hydrogen sites in various materials.

DOI: 10.1103/PhysRevB.91.024102 PACS number(s): 61.05.F−, 61.05.Tv, 88.30.R−

I. INTRODUCTION

As methods of element-selective local structure analysis, x-ray absorption fine structure (XAFS) and electron energy loss spectroscopy (EELS) are commonly used, which employ x-ray and electron beams, respectively. However, a similar method using neutrons does not exist. On the other hand, x-ray fluorescence holography (XFH) [1] and photoelectron holography (PH) [2] have attracted the attention of researchers as they provide more information in local structure analyses, because they can be used to generate three-dimensional (3D) atomic images around specific elements within a range of 3–5 nm. This idea can be applied to neutron holography (NH), which can be used to investigate new fields in solid-state physics via the unique scattering nature of neutrons, such as the higher scattering cross sections for spins and light elements. NH enables the visualization of hydrogen nuclei [3] and is expected in the near future to also visualize the magnetic moments of atoms. These images cannot be obtained by XFH or PH.

Holography was proposed and demonstrated by Gabor in 1948, and its use has become widespread since the invention of the laser. The concept of atomic-resolution holography, exemplified by XFH and PH, was proposed by Szöke in 1986 [4]. Demonstrations of PH [5] and XFH [6] were first performed in 1990 and 1996, respectively. Concerning NH, Cser *et al.* studied its feasibility by calculation in 2000 [7]. Subsequently, Sur *et al.* successfully measured neutron holograms using incoherent scattering from hydrogen atoms [3]. Cser *et al.* also applied NH to the visualization of local structures around hydrogen in palladium [8] and around cadmium in lead [9].

Hayashi, one of the authors of this paper, has studied XFH [1] and recently taken a strong interest in NH owing its high potential for local structure analysis. In 2008, we effectively measured the neutron hologram of palladium hydride using an array of detectors. In our experiment, we observed diffuse scattering, whose intensity was much larger than that of hologram, because the detector could not distinguish between elastically and inelastically scattered neutrons owing to the poor energy resolution. However, we successfully extracted the holographic oscillation from the measured 2D intensity distribution of the neutrons around a $PdH_{0.78}$ single crystal by accurately calculating the diffuse scattering pattern [10]. From this study, we found that the sample should be cooled because the diffuse scattering due to the thermal vibration of atoms is suppressed.

From another viewpoint, Markó and co-workers developed a method that can avoid contamination from Bragg scattering by fixing the scattering angle while changing the sample orientation [8,11]. This method measures a mixture of normal and inverse holograms in principle [12]. To resolve this problem, they also developed a special data processing method termed "double reconstruction."

On the other hand, sample cooling is another effective and practical approach to solving the problem because it can suppress diffuse scattering and enhance holographic signals by reducing the amplitude of the thermal vibration of atoms. Although our setup measures pure normal holograms, the detection of strong diffuse scattering is unavoidable. Therefore, sample cooling is the only means of reducing the intensity of the diffuse scattering.

Here, we measured the holograms and diffuse scattering patterns of the same $PdH_{0.78}$ sample at 300 K and 100 K to investigate the effects of cooling the sample and to obtain high-quality hologram data for realizing the potential of NH.

II. EXPERIMENTAL DETAILS AND DATA PROCESSING

Since the signal-to-background ratio in a hologram is on the order of 10^{-3}, holographic signals are hardly recognized in an experimental hologram. In our previous experiment, we used an array of 150 ^{3}He detectors for hologram measurement to

*khayashi@imr.tohoku.ac.jp

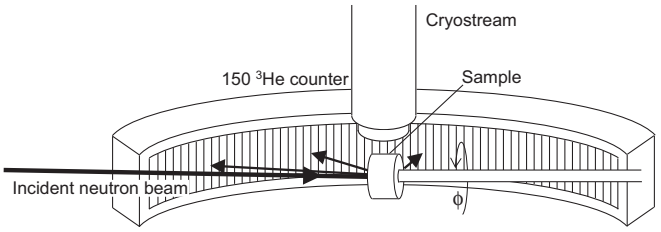

FIG. 1. Schematic drawing of the experimental setup.

reduce the measurement time. This array detector is installed in the neutron powder diffractometer HERMES [13] of the Institute for Materials Research, Tohoku University, at the JRR-3 reactor of the Japan Atomic Energy Agency (JAEA), Tokai, Japan. Figure 1 shows the experimental setup used to record the hologram. The normal to the sample surface was aligned in the direction of the incident neutron beam. The one-dimensional intensity distribution of the scattered neutrons was measured using the 150 ^{3}He detectors, which covered an angular range of $7^\circ \leqslant \theta \leqslant 157^\circ$ with an angular interval of 1° in this experiment. The angular resolution of ϕ was limited to 8° by a slit in front of the 150 ^{3}He detectors. The minimum resolution required to reconstruct the nucleus at 5.4 Å is as small as 5.6° at $\theta = 90^\circ$ (e.g., the required resolution is 8° at $\theta = 45^\circ$ and 135°). Under the present experimental conditions, the nucleus images at 5.4 Å can be clearly reconstructed, as seen from the 110 H image in Fig. 6 in Sec. III B. By scanning ϕ, the 2D intensity distribution was measured. A liquid-nitrogen open-flow cooler (Cryostream) was set above the sample.

As the measured sample, palladium hydride ($PdH_{0.78}$) was used, prepared by the gas phase hydrogenation of a single crystal of palladium metal. The $PdH_{0.78}$ single crystal was 6 mm in diameter and 5 mm in thickness, and electrochemically coated with copper metal to avoid the desorption of hydrogen gas. The mosaicity of the sample was 0.24°, which was confirmed by x-ray diffraction analysis. This sample had the same composition as the sample used by Cser *et al.* in Ref. [8]. An incident neutron beam with a convergence angle of 4.2° was focused on the sample. The wavelength of the neutrons used was 0.18196 nm. The sample was rotated in the ϕ range of 0°–359° in steps of 1°, where the rotation axis was parallel to the incoming beam direction. Neutrons from the sample were detected by the 150 ^{3}He counters at each sample rotation angle. The dwell time at each angle was 840 s. The average intensity at each pixel was about 400 counts. The total count of all the pixels was about 2×10^7. We measured diffuse scattering and hologram patterns at 300 K and 100 K.

The measured data were normalized by the average intensity $I_0(\theta)$. Figure 2(a) shows the raw data of the neutron intensity distribution around the $PdH_{0.78}$ single crystal. The streak patterns along the ϕ direction are sharp Bragg diffractions from an aluminum rod used to support the sample. At $\theta = 48^\circ$ and 81°, barlike diffraction peaks from the $PdH_{0.78}$ single crystal appear at intervals of 90° in ϕ. These distinct patterns at $\theta = 48^\circ$ and 81° are attributed to the 111 and 200 diffraction peaks of $PdH_{0.78}$, respectively. The width of the peaks is about 10°, owing to the poor angular resolution of $\Delta\phi$, but the peaks only appear at $\theta = 48^\circ$ and 81° owing to

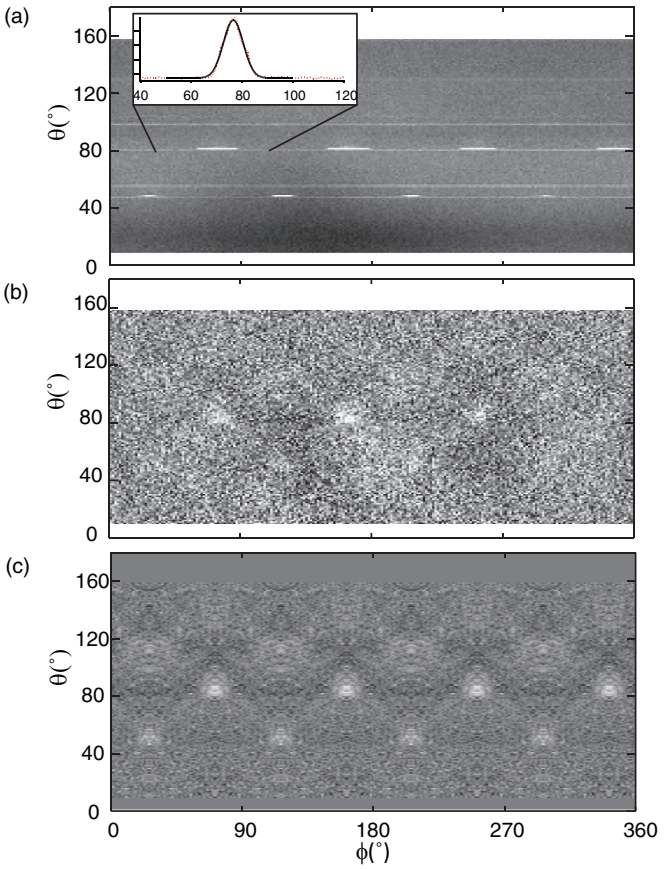

FIG. 2. (Color online) Intensity variations of the observed neutrons as functions of θ and ϕ. (a) Raw data. (b) Data after removal of sharp Bragg peaks from (a). (c) Fourfold-symmetrized data. The inset shows an example of the fitting of a strong diffraction peak.

better resolution of $\Delta\theta \sim 0.5^\circ$. They were eliminated carefully by Gaussian fitting, as shown in the inset of Fig. 2(a), to obtain the patterns in Fig. 2(b). In this pattern in Fig. 2(b), broad peaks were also observed at ϕ intervals of 90° at $\theta = 81^\circ$. We clearly see the fourfold symmetry of the diffuse scattering pattern. The average intensity at each pixel is about 250 counts. Since this value is too low to extract a hologram pattern whose amplitude is on the order of 10^{-3} relative to the background intensity, the data are fourfold-symmetrized as shown in Fig. 2(c). Here, we can recognize the crystallographic orientation of the sample from the Bragg diffractions of $PdH_{0.78}$. Since the amplitude of the displayed pattern is on the order of 10^{-2}, it mainly originated from the diffuse scattering.

III. RESULTS AND DISCUSSION

A. Diffuse scattering

To reduce the overlap of diffuse scattering due to the thermal vibration of atoms, we cooled the sample to 100 K and measured the neutron intensity distribution around the sample. Figures 3(a) and 3(b) show 2D maps of the neutron intensity at 300 K and 100 K, respectively. Here, the data at 300 K are the same as those in Fig. 2(c) but are low-pass-filtered to reduce noise. In Fig. 3(a), bright spots are observed at $\theta = 81^\circ$ and 48°. From Fig. 3(b), the whole pattern observed at 100 K

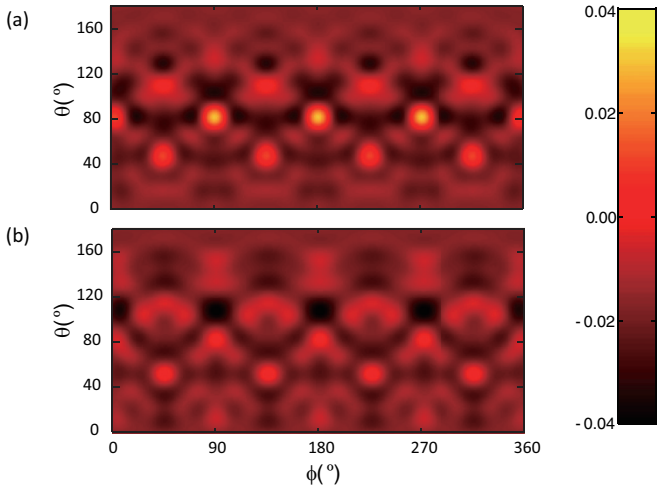

FIG. 3. (Color online) Intensity variations of the observed neutrons at (a) 300 K and (b) 100 K. The data are low-pass-filtered. The values of θ are shifted by 18° from those in Fig. 2 to adjust the crystallographic orientation.

is weaker than that at 300 K, particularly the spot intensities at $\theta = 81°$, indicating that cooling the sample is effective for reducing the overlap of diffuse scattering.

Next, we consider the observed diffuse scattering patterns. Kopecky *et al.* calculated x-ray intensity distributions resulting from thermal diffuse scattering from single crystals [14]. When u_i is the small instantaneous displacement of each nucleus, the diffuse component of the scattering intensity is given by

$$I_{\text{diff}} = \frac{I_0}{R^2} \sum_{i=1}^{N} \sum_{j=1}^{N} b_i \exp(-M_i) b_j^* \exp(-M_j) \times \exp[-i(\mathbf{k} - \mathbf{k_0})(\mathbf{r} - \mathbf{r_i})][\exp(k^2 \langle u_i u_j \rangle) - 1], \quad (1)$$

where $M_i = k^2 \langle u_i^2 \rangle$, $M_j = k^2 \langle u_j^2 \rangle$, and $\mathbf{k}_0$ is the incoming beam vector. The thermal vibrations of distant nuclei are less correlated; therefore, $\langle u_i u_j \rangle$ approaches zero with increasing distance between nuclei i and j. Utilizing this equation, we can calculate the diffuse scattering pattern using a 264-nucleus PdH cluster.

The amplitudes of u_i for Pd at 300 K and 100 K can be obtained using the one-phonon process [15]. We obtained 0.074 Å and 0.044 Å at 300 K and 100 K, respectively. These values are similar to those obtained using Debye's formula, which gives the relationship between u_i and the Debye temperature [16]. (The Debye temperature of Pd is $T_D =$ 275 K.) In the estimation, we calculated the Debye-Waller factor, which is proportional to u_i^2, using the one-phonon density of states based on the definitions in Ref. [17], assuming that the acoustic mode with the Debye spectrum as the density of states, $Z(\omega)$, is proportional to $3\omega^2/\omega_D$, where ω and ω_D are the phonon frequency and Debye frequency, respectively. The Debye frequency can be obtained by $\omega_D = kT_D/\hbar$. Since Worsham *et al.* reported u_i to be 0.071 Å at room temperature from the x-ray diffraction result of $PdH_{0.706}$, our estimated values are considered to be in agreement with the actual values [18].

Using these parameters and Eq. (1), we calculated the diffuse scattering pattern. Here, we introduce the correlation effect [19] for fitting the calculated patterns to the experimental ones. The correlation effect is defined by

$$\tau_{ij} = \langle u_i u_j \rangle / \left(\langle u_i^2 \rangle + \langle u_j^2 \rangle \right). \quad (2)$$

The diffuse scattering patterns at 300 K and 100 K were obtained by normalizing the measured intensities by the background intensity, which was mainly due to incoherent scatterings from hydrogen nuclei. Therefore, the theoretical amplitudes must also be normalized by the calculated intensity of the incoherent scattering, which can be expressed by

$$I_{\text{inc}} = \frac{I_0}{R^2} \sum_{i=1}^{N} b_{inc,i}^2, \quad (3)$$

where $b_{inc,i}$ is the incoherent scattering length of a hydrogen nucleus. I_{inc} was easily calculated and then the theoretical intensities of the spots could be normalized.

We attempted to obtain the value of the correlation effect for each pair by fitting the calculated diffuse scattering pattern to the experimental pattern. The used values of u_{Pd} and u_{H} were 0.074 Å and 0.23 Å, respectively. The former value was obtained earlier in this section. And the latter value was reported by Worsham *et al.* [18]. For the pattern at 300 K in Fig. 3(a), the values of $\tau_{\text{Pd-Pd}}$ for the first-, second-, third-, and fourth-neighbor Pd-Pd pairs were estimated to be 0.64, 0.58, 0.51, and 0.08, respectively. Other correlation effects were negligibly weak. $\tau_{\text{Pd-Pd}}$ rapidly decreases at the distance of the fourth-neighbor Pd-Pd pair.

Next, we estimated the values of the correlation effect from the diffuse scattering data at 100 K. The used value of u_{Pd} was 0.046 Å which was calculated earlier in this section. We could not find the experimental data of u_{H} at 100 K, whereas there are u_D data for deuterium in palladium at this temperature. Using the data, we circumvented to need to obtain u_{H} at 100 K for the calculation of diffuse scattering. In the report by Lawson *et al.* [20], the values of u_D at 100 K and 300 K are 0.16 Å and 0.20 Å respectively, indicating a reduction rate of 0.8. Applying this rate to $u_{\text{H}} = 0.23$ Å at 300 K, we could obtain $u_{\text{H}} = 0.18$ Å at 100 K. We adopted this value for the diffuse scattering calculation at 100 K. The obtained values of $\tau_{\text{Pd-Pd}}$ are listed in Table I.

The values of $\tau_{\text{Pd-Pd}}$ at 100 K are approximately 1.5 times higher than those at 300 K. The distance dependence of $\tau_{\text{H-H}}$ is similar to that of the $\tau_{\text{Pd-Pd}}$, and the ratios of $\tau_{\text{H-H}}$ to $\tau_{\text{Pd-Pd}}$ are approximately 0.2. The parameters in Table I are considered to reflect the coupling state between H and Pd in a $PdH_{0.78}$ single crystal. The calculated patterns using these parameters are displayed in Fig. 4.

The patterns in Figs. 4(a) and 4(b) are similar to those in Figs. 3(a) and 3(b), respectively. In particular, the spots observed at $\theta = 81°$ and 48° are well reproduced. Since the values of $\tau_{\text{H-H}}$ and $\tau_{\text{Pd-H}}$ are zero for the calculation of the pattern at 300 K, it is known that the motions of the hydrogen atoms in the acoustic modes contribute very little to the formation of the diffuse scattering. In contrast, the hydrogen atoms vibrate with a large amplitude (0.24 Å) in the optical mode [21] because optical phonons have been observed even at room temperature [22]. However, the contribution of optical

TABLE I. Values of correlation effects.

	Pd-Pd$_{1st}$	Pd-Pd$_{2nd}$	Pd-Pd$_{3rd}$	Pd-Pd$_{4th}$	H-H$_{1st}$	H-H$_{2nd}$	H-H$_{3rd}$	H-H$_{4th}$	Pd-H$_{1st}$	Pd-H$_{2nd}$
300 K	0.64	0.58	0.53	0.08						
100 K	0.94	0.80	0.70	0.14	0.19	0.17	0.15	0.02	0.09	0.03
Distance (Å)	2.89	4.08	5.00	5.77	2.89	4.08	5.00	5.77	2.04	4.56

phonons to diffuse scattering should be negligible compared with that of the acoustic phonons considered in the present discussion because the lower energy limit of optical phonons is approximately 1.5 times larger than that at the Debye temperature [15]. Note that the diffuse scattering intensity is inversely proportional to ω.

On the other hand, in the experimental diffuse scattering pattern at 100 K in Fig. 3(b), spots at $\theta = 81^\circ$ are very week but the spots at $\theta = 48^\circ$ remain. By giving the certain values to $\tau_{\text{H-H}}$ and $\tau_{\text{Pd-H}}$ in Table I, we could reproduce the resemble pattern, as shown in Fig. 4(b). Thus, it is clarified that the Pd-H coupling is more rigid at lower temperatures, although hydrogen in Pd is easily desorbed at 300 K. $\tau_{\text{Pd-H}}$ and $\tau_{\text{H-H}}$ correspond directly to the stability of hydrogen in Pd bulk.

B. Holography

Our original aim in the present experiment was to suppress diffuse scattering and enhance hologram signals by cooling the sample. As shown in Fig. 3, we succeeded in reducing the intensity of diffuse scattering. Moreover, diffuse scattering patterns were precisely calculated in the previous section. We attempted to extract a pure hologram from the data observed at 300 K and 100 K by subtracting the calculated diffuse scattering pattern. After the subtraction, the hologram data were symmetrized and extended to a 4π sphere, as shown in Fig. 5. Such data handling increases the statistical accuracy of the hologram data and the range in **k**-space, where **k** is the wave number vector [23]. Compared with the recently measured XFH holograms [1], the neutron hologram is noisy, and distinct Kossel lines [24] cannot be seen owing to the weakness of the incident neutron beam; the neutron flux was several orders of magnitude lower than that of a synchrotron radiation x-ray beam.

As a general method of real-space reconstruction for single-wavelength holograms, we previously used the Helmholtz-Kirchhoff formula [25]. However, here we used the Barton multiple-wavelength holography reconstruction formula [26], which was modified from the Helmholtz-Kirchhoff formula. Whereas the sign of the x-ray scattering factor of each element is always the same, the sign of the neutron scattering length varies with the isotope. For example, the scattering lengths of natural H and Pd nuclei are negative and positive, respectively. The nucleus images reconstructed using the Barton formula should represent the signs of the scattering lengths for each isotope because they correctly visualize the phase shift of the scattering as the phase of the atomic image.

Defining $\chi(\mathbf{k})$ as the hologram, the Barton formula can be written as

$$U(\mathbf{r}) = e^{ikr} \iint e^{-ikr} \chi(\mathbf{k}) d\sigma, \tag{4}$$

where $d\sigma$ is a unit on the surface of the hologram. Applying Eq. (4) to 4π holograms at 300 K and 100 K, we reconstructed real-space images. Figures 6(a) and 6(b) show nucleus images of the (001) plane at 300 K and 100 K, respectively. Markó *et al.* have estimated the total number of neutrons required to reconstruct nucleus images and suggested that a highly noisy hologram, where no holographic oscillations are observed, can also provide visible atomic images [11]. On the basis of the formulas described in Ref. [11], error bars were estimated as

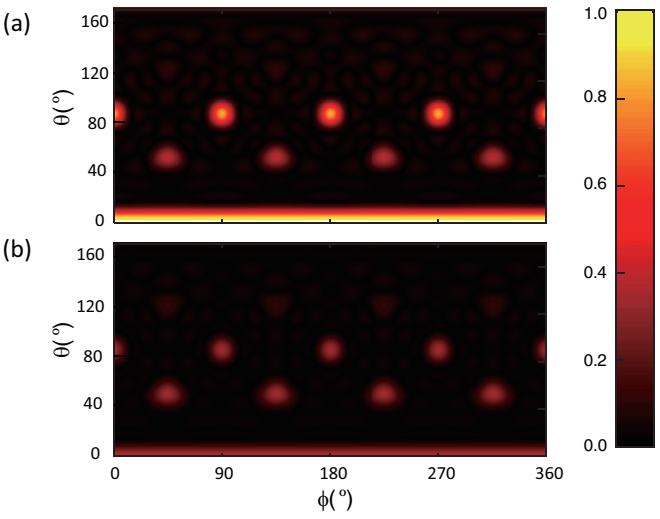

FIG. 4. (Color online) Intensity variations of the calculated diffuse scattering pattern. (a) Calculation with only the Pd cluster. (b) Calculation with the PdH cluster. The data were not low-pass-filtered, in contrast to the data in Fig. 3.

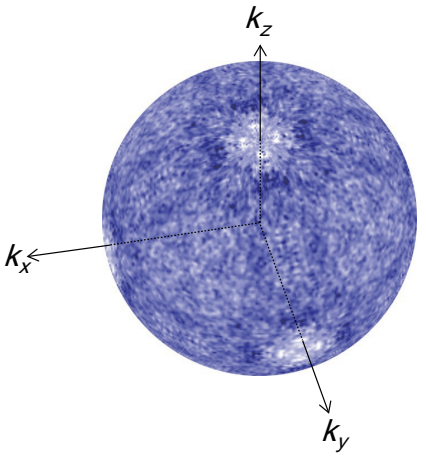

FIG. 5. (Color online) Neutron hologram of PdH$_{0.78}$ in the reciprocal space. The coordinate axes are shown.

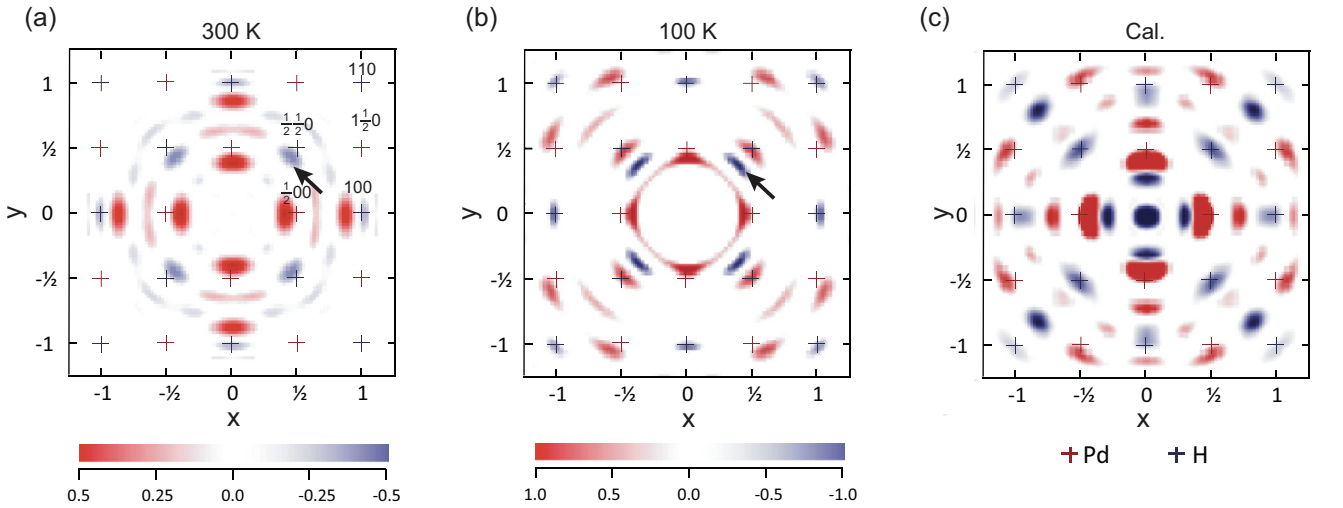

FIG. 6. (Color) Nucleus images of (001) plane. H is located at the center of each figure. Red and blue respectively indicate positive and negative values of the real part of the Fourier transform. (a) and (b) Reconstructions from experimental holograms obtained at 300 K and 100 K, respectively. The range of the contrast bar in (b) is twice that in (a). (c) Reconstruction from theoretical hologram. The arrows in (a) and (b) indicate the H image. The axes of reduced units are used here. The lattice constant of PdH is $a = 4.08$ Å

shown later in Fig. 7. The images display only the real part of the reconstruction and they reflect the scattering lengths. Here, the positive and negative peaks should appear at the Pd and H positions because the scattering lengths of Pd and H are 5.91×10^{-15} m and -3.739×10^{-15} m, respectively. In Fig. 6(a), the neighboring Pd image at the $\frac{1}{2}00$ position is observed as positive peaks, and the image at the $\frac{1}{2}\frac{1}{2}0$ H position is weakly observed as negative peaks, as indicated by the arrow. Therefore, the reconstructions of these neighboring Pd and H nucleus images are successful, although they are shifted toward the center. Moreover, a faint negative peak appears at the 100 H position. However, distinct images cannot be seen at more distant positions.

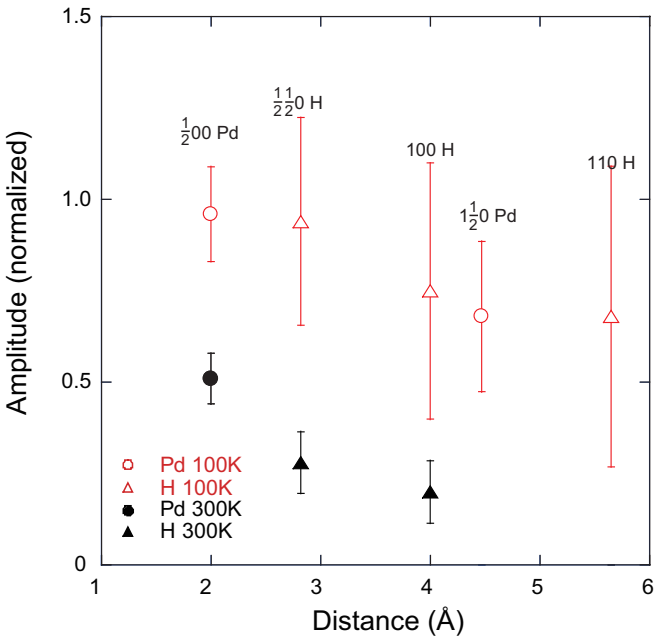

FIG. 7. (Color online) Plots of image amplitude as a function of the distance from the H. All the amplitudes are normalized by the highest amplitude of the $\frac{1}{2}00$ Pd image at 100 K. The open and closed symbols indicate the amplitudes at 300 K and 100 K, respectively. The circles and triangles indicate the amplitudes of H and Pd, respectively.

On the other hand, in the reconstruction for 100 K shown in Fig. 6(b), red and blue spots respectively appear at the theoretical positions of Pd and H at further positions. Moreover, all the observed images become sharper along the radial direction. Although the red spots appear exactly at $\frac{1}{2}\frac{1}{2}0$ H position, we consider that the blue spots observed slightly nearer the center constitute the true H image, indicated by the arrow. The position of this image is consistent with that in Fig. 6(a). The other images clearly represent Pd and H as the red and blue spots, respectively.

To verify the validity of the experimental atomic images, we calculated the hologram using a 264-nucleus PdH cluster with a rocksalt-type crystal structure. Figure 6(c) shows the nucleus images reconstructed from the calculated hologram. Compared with the images in Fig. 6(b), there are many artifacts, but red and blue spots appear at the theoretical positions of Pd and H, respectively, similarly to the experimental images in Fig. 6(a). All first-neighbor Pd nucleus images in Figs. 6(a), 6(b), and 6(c) were reconstructed close to the center, namely, a similar tendency can be observed. On the other hand, unlike the experimental images, the theoretical H image at the $\frac{1}{2}\frac{1}{2}0$ position appears at the ideal position and the theoretical 100 H image appears at a position closer to the center.

The comparison between the images in Figs. 6(a) and 6(b) clearly indicates that the low-temperature holography experiments effectively enhance the visibility of the images, particularly images of distant nuclei such as $1\frac{1}{2}0$ and 110 nuclei. To show the tendency of the visibility with increasing distance from the center, the amplitudes of the observed images in Figs. 6(a) and 6(b) are plotted as a function of the distance from the center as shown in Fig. 7. The H image amplitudes are inverted because they are negative in Fig. 6. The amplitude

of the neighboring Pd nucleus is increased twofold by sample cooling to 100 K. Moreover, the H images became distinct at 100 K, whereas they could hardly be seen at 300 K. Thus, we successfully demonstrated the sample cooling effect on nucleus images, particularly hydrogen images.

To quantitatively understand how the images were improved by sample cooling, we estimated the relation between image visibility and nucleus fluctuation by calculating a hologram while changing the mean square displacement of the nuclei σ. The solid curve in Fig. 8 indicates the σ dependence of the image amplitude. Note that σ is a similar parameter to u_i. However, σ is the mean square displacement relative to the central H while u_i is that relative to the average position. In our calculation, we used a H-H dimer model, where one H nucleus is an emitter and the other is a scatterer. The interatomic distance between them is 4 Å. We have confirmed that the σ dependence of the normalized image amplitude is not dependent on the interatomic distance or a type of scatterer nucleus, such as the H or Pd nucleus [27].

In the following discussion, we show that the enhancement of the images can be explained quantitatively by the fluctuation amplitudes of the nuclei based on the calculation in Fig. 8. The value of 0.23 Å was used for σ_{H} at 300 K [18]. However, if we apply some parameters of the nucleus fluctuations to the curve in Fig. 8, we must use the convoluted value of two σ_{H}, $\sigma_{\mathrm{H\text{-}H}} = \sqrt{0.23^2 + 0.23^2} = 0.33$ Å, because both the central and scatterer H nuclei fluctuate similarly. Note that all the images obtained using the hologram correlate with the central H nucleus. That is, the fluctuation of the central H atom reduces

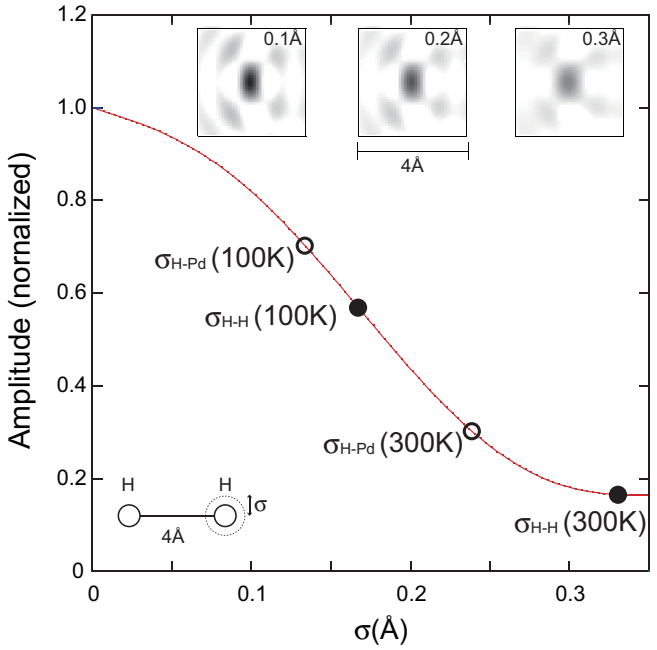

FIG. 8. (Color online) Dependence of image amplitude on the nucleus fluctuation. The amplitude is normalized by its highest value at $\sigma = 0$ Å. $\sigma_{\mathrm{H\text{-}H}}$ is the convolution of two σ_{H}. $\sigma_{\mathrm{H\text{-}Pd}}$ is the convolution of σ_{H} and σ_{Pd}. The inset at the lower left indicates the dimer H-H model calculated in the hologram calculations. The insets at the upper top indicate the nucleus images reconstructed from the calculated holograms with $\sigma = 0.1$ Å, 0.2 Å, and 0.3 Å.

the amplitude of all the reconstructed images. $\sigma_{\mathrm{H\text{-}H}} = 0.33$ Å gives an amplitude of 0.16 in Fig. 8, which is plotted using a closed circle on the solid line. On the other hand, the ratio of the experimental amplitude at 100 K to that at 300 K is 0.29 for the $\frac{1}{2}\frac{1}{2}0$ H nucleus from Fig. 7. Using this amplitude ratio, the amplitude at 100 K in Fig. 8 can be estimated to be 0.55, indicated by another closed circle. At this point, $\sigma_{\mathrm{H\text{-}H}}$ becomes 0.17 Å; this gives $\sigma_{\mathrm{H}} = 0.12$ Å by deconvolution. The obtained σ_{H} at 100 K is approximately half of that at 300 K and is different from $u_{\mathrm{H}} = 0.18$ Å at 100 K. However, u_{H} is the displacement relative to the central H position. Since some atoms vibrated together with neighboring H atoms, this should reduce the value of σ_{H}.

To confirm the accuracy of the above estimation of σ_{H}, we discuss the amplitudes of the $\frac{1}{2}00$ Pd image in the same way. The values of σ_{Pd} can mostly be regarded as being the same as those of u_i for Pd, which have been estimated to be 0.046 Å and 0.074 Å at 100 K and 300 K, respectively. Therefore, the convolution of σ_{H} and σ_{Pd}, $\sigma_{\mathrm{H\text{-}Pd}}$, is 0.13 Å and 0.24 Å for 100 K and 300 K, respectively. The amplitudes of the Pd images at 100 K and 300 K on the curve in Fig. 8 can be obtained from the values of $\sigma_{\mathrm{H\text{-}Pd}}$ at 100 K and 300 K, respectively, as plotted by the open circles. Thus, the amplitude ratio of the Pd images at 100 K and 300 K in Fig. 8 can be estimated to be 0.42. The experimental ratio is 0.53 from the amplitudes of the $\frac{1}{2}00$ Pd nuclei in Fig. 7. Taking into account the large errors of the experimental image amplitude, they appear to be in reasonable agreement. Therefore, the estimated values of σ_{H} can be explained by the change in amplitude of the Pd images.

In the calculation of the hologram, we did not take into account the vibrations of the nuclei. However, the real-space images obtained from the experimental and theoretical holograms show the same features. As expected, there are some discrepancies caused by the insufficient number of atoms in the cluster and the lack of an extinction effect in the hologram calculation, in addition to the effect of data processing. Moreover, there are still unnecessary oscillations even after subtracting the diffuse scattering pattern from the measured data. However, these problems will be resolved by recording holograms using neutron beams with several different wavelengths.

Hydrogen atoms form short-range-ordered Ni_2Mo, Ni_3Mo, and Ni_4Mo structures at low temperatures [28], and the Ni_2Mo structure should enhance the 100 H image. Concerning 110 H, since the experimental amplitude is high compared with the calculated value, this effect might be observed. Since such a structure is fully developed at 50 K, hologram measurement at this temperature is promising.

The holograms of the PdH system have already been measured by Cser's group in Hungary [8]. Recently, they have also reconstructed distinct H and Pd images up to third-neighbor atoms using nucleus scattering lengths of both signs [29]. We confirmed this feature of NH in a wider real-space range. This characteristic of NH gives it a major advantage over XFH and PH, in which the elements of atomic images are evaluated only from their amplitude. To date, all studies on NH have been carried out using single-wavelength holography, mainly owing to the weakness of the neutron sources. However, multiple-wavelength NH experiments will enable us to more easily distinguish the elements, particularly hydrogen.

IV. CONCLUSION

NH is a relatively new method among several atomic-resolution holography methods. Since it enables local structure analysis around H, it is regarded as a promising analytical method for hydrogen storage materials. On the other hand, incoherently scattered neutrons cannot be distinguished from diffracted neutrons. The thermal vibration of a nucleus precludes a pure hologram from being obtained because it causes the reduction of holographic signal intensity as well as thermal diffuse scattering. Therefore, in the present experiment, we cooled a sample to enhance its holographic signals and suppress thermal diffuse scattering. The diffuse scattering pattern at 100 K was markedly different from that at 300 K, indicating the significant modification of the hydrogen lattice dynamics. The hologram data at 100 K, which were obtained by subtracting the diffuse scattering pattern, provide images of H and Pd nuclei as negative and positive peaks, respectively. Taking into account the fact that the H images are faintly visible in the reconstruction at 300 K, sample cooling is very effective for observing them. These features are important for the determination of hydrogen sites in materials.

Because single-wavelength holography was carried out, the reconstruction lacked some neighbor atoms and had relatively many artifacts. However, very high quality atomic images are expected to be obtained by performing multiwavelength NH experiments over a wide wavelength range using strong spallation neutron sources. Recently, it has been found that XFH in a multiwavelength mode is promising for estimating local lattice distortions [27,30] and finding nanoclusters [31] in crystals. However, one disadvantage of XFH is the difficulty in imaging light atoms such as oxygen and hydrogen owing to their low scattering powers for x rays. Since multiwavelength NH can reconstruct light atoms as well as heavy atoms, it will be a very powerful technique for the analysis of oxide semiconductors and superconductors. Moreover, NH can use the nature of magnetic scattering to reconstruct the magnetic moments of each atom. By performing such reconstructions, NH will greatly contribute to the fields of magnetic materials and spintronics.

ACKNOWLEDGMENTS

We thank Dr. Ohwada for the helpful discussion on the features of diffuse scattering. We also thank Dr. Ohkawa for his technical assistance. We would also like to acknowledge JSPS KAKENHI Grants No. 25286040, No. 24656367, and No. 24656004. This work was carried out at beamline T1-3 of JRR-3 (Proposals No. 6694 and No. 7744).

[1] K. Hayashi, N. Happo, S. Hosokawa, W. Hu, and T. Matsushita, J. Phys.: Condens. Matter **24**, 093201 (2012).
[2] T. Matsushita, F. Matsui, H. Daimon, and K. Hayashi, J. Electron Spectrosc. Relat. Phenom. **178/179**, 195 (2010).
[3] B. Sur, R. B. Rogge, R. P. Hammond, V. N. P. Anghel, and J. Katsaras, Nature (London) **414**, 525 (2001).
[4] A. Szöke, in *Short Wavelength Coherent Radiation: Generation and Applications, March 1986, Monterery*, edited by D. T. Attwood and J. Bokor, AIP Conf. Proc. No. 147 (AIP, New York, 1986), p. 361.
[5] G. R. Harp, D. K. Saldin, and B. P. Tonner, Phys. Rev. B **42**, 9199 (1990).
[6] M. Tegze and G. Feigel, Nature (London) **380**, 49 (1996).
[7] L. Cser, G. Krexner, and Gy. Török, Europhys. Lett. **54**, 747 (2001).
[8] L. Cser, Gy. Török, G. Krexner, M. Prem, and I. Sharkov, Appl. Phys. Lett. **85**, 1149 (2004).
[9] L. Cser, G. Krexner, M. Markó, I. Sharkov, and Gy. Török, Phys. Rev. Lett. **97**, 255501 (2006).
[10] K. Hayashi, K. Ohoyama, S. Orimo, Y. Nakamori, H. Takahashi, and K. Shibata, Jpn. J. Appl. Phys. **47**, 2291 (2008).
[11] M. Markó, L. Cser, G. Krexner, and Gy. Török, Meas. Sci. Technol. **20**, 015502 (2009).
[12] N. Happo, K. Hayashi, and S. Hosokawa, Jpn. J. Appl. Phys. **49**, 116601 (2010).
[13] K. Ohoyama, T. Kanouchi, K. Nemoto, M. Ohashi, T. Kajitani, and Y. Yamaguchi, Jpn. J. Appl. Phys. **37**, 3319 (1998).
[14] M. Kopecky, E. Busetto, and A. Lausi, J. Appl. Crystallogr. **36**, 1368 (2003).
[15] J. M. Rowe, J. J. Rush, H. G. Smith, M. Mostoller, and H. E. Flotow, Phys. Rev. Lett. **33**, 1297 (1974).
[16] B. D. Cullity, *Elements of X-Ray Diffraction*, 2nd ed. (Addison-Wesley Publishing, Reading, Massachusetts, 1978).
[17] S. W. Lovesey, *Theory of Neutron Scattering from Condensed Matter*, Vol. 1 (Oxford Science Publications, New York, 1984), Chap. 4.
[18] J. E. Worsham, Jr, M. K. Wilkinson, and C. G. Shull, J. Phys. Chem. Solids **3**, 303 (1957).
[19] T. Sakuma, J Phys Soc. Jpn. **61**, 4041 (1992).
[20] A. C. Lawson, J. W. Conant, R. Robertson, R. K. Rohwer, V. A. Young, and C. L. Talcot, J. Alloys Compd. **183**, 174 (1992).
[21] J. Bergsma and J. A. Goedkoop, Physica **26**, 744 (1960).
[22] B. M. Geerken, R. Griessen, L. M. Huisman, and E. Walker, Phys. Rev. B **26**, 1637 (1982).
[23] M. Tegze, G. Faigel, S. Marchesini, M. Belakhovsky, and A. I. Chumakov, Phys. Rev. Lett. **82**, 4847 (1999).
[24] B. Sur, R. B. Rogge, R. P. Hammond, V. N. P. Anghel, and J. Katsaras, Phys. Rev. Lett. **88**, 065505 (2002).
[25] J. J. Barton, Phys. Rev. Lett. **61**, 1356 (1988).
[26] J. J. Barton, Phys. Rev. Lett. **67**, 3106 (1991).
[27] S. Hosokawa, N. Happo, T. Ozaki, H. Ikemoto, T. Shishido, and K. Hayashi, Phys. Rev. B **87**, 094104 (2013).
[28] O. Blaschko, P. Fratzl, and R. Klemencic, Phys. Rev. B **24**, 277 (1981).
[29] M. Markó, G. Krexner, J. Schefer, A. Szakál, and L. Cser, New J. Phys. **12**, 063036 (2010).
[30] S. Hosokawa, N. Happo, and K. Hayashi, Phys. Rev. B **80**, 134123 (2009).
[31] W. Hu, K. Hayashi, T. Yamamoto, N. Happo, S. Hosokawa, T. Terai, T. Fukuda, T. Kakeshita, H. Xie, T. Xiao, and M. Suzuki, Phys. Rev. B **80**, 060202(R) (2009).